A Variable Stiffness Spherical Joint Motor by Magnetic Energy Shaping

Mengke Li ⬤, Qianhong Xiao ⬤, Zehui Wang ⬤, Chenjie Liu ⬤, and Kun Bai ⬤, *Member, IEEE*

Abstract—This article presents a robotic joint motor capable of providing bio-joint-like motion and controllable stiffness in omnidirection. Unlike existing compliant actuators relying on elastic elements or force/impedance control, the output shaft of the proposed actuator can be stabilized at any equilibrium in antagonistic sense by purely manipulating the motor currents in the electromagnets distributed on the spherical surface of the joint socket. The multi-DOF orientation and the joint stiffness can be simultaneously adjusted by dynamically shaping the magnetic energy of the motor in the vicinity of any specified equilibrium. The relationship between the motor currents and the motor torque as well as the torque gradients is established in closed-form for the spherical joint motor (SJM), which allows for real-time shaping of the magnetic energy and manipulation of the equilibrium and the stiffness. The concept of the proposed variable stiffness motor with the energy shaping method have been validated as a robotic wrist equipped on a robotic manipulator. The results demonstrate that the SJM is capable of providing dexterous motion and intrinsic joint compliance in omnidirection while also allowing simple joint design and efficient compliant manipulations for robots.

Index Terms—Compliant actuator, robotic joint, spherical motor, variable stiffness actuator.

I. Introduction

IN ORDER for robots to work safely and efficiently in the vicinity of human operators in unstructured environment, joint compliance is one of the major trends in next generation robotic manipulators [1], [2], [3]. While compliant behaviors can be realized through torque sensing and control, intrinsic compliance enables more robust behavior for robots [4]. Existing solutions deliver intrinsic joint compliance basically through elastic elements incorporated with motors to provide controllable joint motion and adjustable stiffness [5]. The elastic elements as well as the stiffness adjusting mechanisms usually lead to complex structures leading to increased moment of inertia

and unwanted mechanical backlashes/frictions. The complexities will even increase dramatically when multi-DOF joints are required for a robot to perform complex tasks. It is desired that robotic joint actuators featured with simple structure, dexterous motion as well as intrinsic joint compliance are developed to ensure compliant robotic manipulations in a wider range of applications.

Compliant actuators are becoming increasingly important for robots in emerging applications, such as cooperative robots, rehabilitative robots and legged robots, where the tasks cannot be explicitly defined in geometry because of the unstructured environment or unpredictable human interactions [6]. Existing compliant manipulations can be achieved in two ways: active impedance control and intrinsic compliance. Active impedance control basically manipulates the robotic joint torque to achieve desirable dynamic relationship between the motion variables and the contact forces during interactions [7], which is akin to implementing a virtual spring and/or damper with desired impedance/admittance in the interface between robot links and objects/humans. The implementation of active impedance control primarily relies on force/torque feedback control [8], [9]. Since a torque loop is usually required in impedance control, the torque sensing bandwidth/noise and the torque control stability usually restrict the dynamic capability and robustness during contact. Prior knowledge about the target stiffness is usually required to ensure stable interaction and abrupt impacts can also lead to instability for the feedback system [1]. Compliant actuators, such as serial elastic actuators and variable stiffness actuators, are composed of elastic elements (such as torsional springs) and stiff motors in robotic joints. Compliant actuators which provide intrinsic compliance with the elastic elements instead of force/torque control to avoid hard contact provide better robustness to impacts [10], better energy efficiency [11] and increased dynamic bandwidth [12]. As elastic elements usually have fixed stiffness which lacks the capability of flexibly adapting to the tasks, a variety of mechanisms have been proposed to alter the joint stiffness [13], [14], [15], [16] to achieve better task adaptability. In order to simultaneously adjust the robot link positions and the stiffness, at least two motors are usually required in each joint. Therefore, robotic joints equipped with compliant actuators can prevent instability during contact, but at the cost of increased complexity in their structure. As robotic manipulators need to possess movement and adjustable stiffness in all directions to interact with unstructured environments, there still exists significant challenge to design compliant actuators that can enable agile motion with simple structure

while also fulfilling complex robotic manipulations and variable compliance in omnidirections.

A flurry of research efforts have been conducted to design novel actuators to provide dexterous motions and compliant manipulations for robots. Among them are the spherical motors capable of multi-DOF rotational motions in one joint and direct-drive torque manipulations of robot links [17], [18], [19], [20]. Spherical motors utilize the interactions between the electromagnets (EMs) and permanent-magnets (PMs) distributed on the spherical surfaces of a socket-like rotor and a ball-like stator, which provides a bio-joint-like structure for robotic actuators to render complex motion while maintaining concise design. In [2], a back-drivable spherical wrist with smart compliance for rendering human wrist-like capabilities in robotic applications was presented; and active impedance control was proposed for this wrist motor to synthetically impose both motion accuracy and active compliance for dedicated wrist manipulations. Even though the spherical wrist in [2] has shown superior performances in dexterous motions and compliant manipulations, it is still beneficial for robot joints to avoid the restrictions on system stability and robustness in interactive tasks owing to active impedance control. Therefore, this article proposes a spherical joint motor (SJM) with adjustable intrinsic compliance from actuation perspective (instead of control-level) to offer robotic manipulations with better robustness and task adaptability while still retaining the structural simplicity for rendering multi-DOF motions and the direct-drive capability. The reminder of this article offers the followings.

1) The concept of a SJM with variable stiffness in omnidirection is introduced. An energy shaping method for controlling the equilibrium and stiffness of the SJM to provide intrinsic joint compliance without any elastic elements is proposed. It is shown that a convex magnetic energy field with the lowest energy at any desired equilibrium can be formed by manipulating the motor currents. Unlike conventional motors where the current inputs are only used to control motor torque, a closed-form relationship between the current inputs and motor torque as well as torque gradient are derived in this article. Hence, the currents can be used to adjust both motor torque and torque gradient, which allows shaping of the magnetic field to control the equilibrium and the joint stiffness of the SJM.

2) The feasibility of the SJM as an intrinsic compliant joint is validated on a cooperative robotic manipulator where the SJM functions as an omnidirectional wrist with variable stiffness. The performance of the SJM with energy shaping method is compared to conventional active impedance control, which show that the proposed method is capable of providing intrinsic joint compliance with better robustness and adaptability to unstructured environment. The feasibility of the SJM wrist for performing peg-in-hole operations and shape/stiffness perception of unstructured targets have also been demonstrated. The SJM capable of dexterous motion and variable stiffness in omnidirection with simple joint design show great potentials in compliant robotic manipulations.
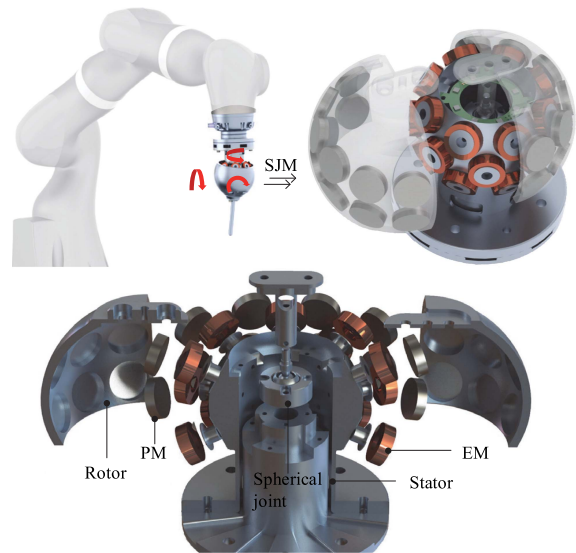

Fig. 1. Design concept of a SJM for robots.

II. A VARIABLE STIFFNESS SJM WITH ENERGY SHAPING

Fig. 1 illustrates a bio-joint-like SJM designed for robotic manipulators featured with dexterous motions and compliant interactions. As detailed in Fig. 1, the stator and rotor of the SJM consist of electromagnets (EMs, housed on the outer surface of the stator) and permanent magnets (PMs, embedded in the rotor) respectively. The PMs and EMs distribute on two concentric spherical surfaces with their axes pointing radially. The rotor is supported through a low friction spherical rolling joint (*SRJ006C, Hephaist*) which allows omnidirectional rotations in one joint. The SJM is directly actuated by the electromagnetic interactions between the PMs and the EMs. When the EMs are supplied with current inputs, the magnetic energy in the EMs and PMs leads to a three-dimensional magnetic torque τ on the rotor, which translates into three-DOF rotations.

Fig. 2 presents the principle of the proposed magnetic energy shaping method of the SJM for realizing variable joint stiffness. As illustrated in Fig. 2(a), the shape of the magnetic energy can be controlled in the vicinity of any arbitrary orientation with a set of current inputs in the EMs. When a convex magnetic energy field is formed with the desired equilibrium orientation ($\mathbf{q}_e$) being the lowest energy point, the rotor shaft can be regulated at the equilibrium in an antagonistic sense without any feedback control or elastic elements. When the rotor shaft is pushed away from the equilibrium by external forces/torques, the magnetic torque (due to the restored magnetic energy) tends to push back the shaft to the equilibrium (similar to a set of antagonistic springs as illustrated in Fig. 2(a)) where the stiffness can be adjusted by configuring the gradient of the energy field. The equilibrium and the stiffness can be independently controlled and in omnidirection due to the spherical joint configuration.

A. Antagonistic Torque by Magnetic Energy Shaping

Fig. 2(b) schematically presents the coordinate systems of the SJM and the pole configuration where *XYZ* and *xyz* represent the
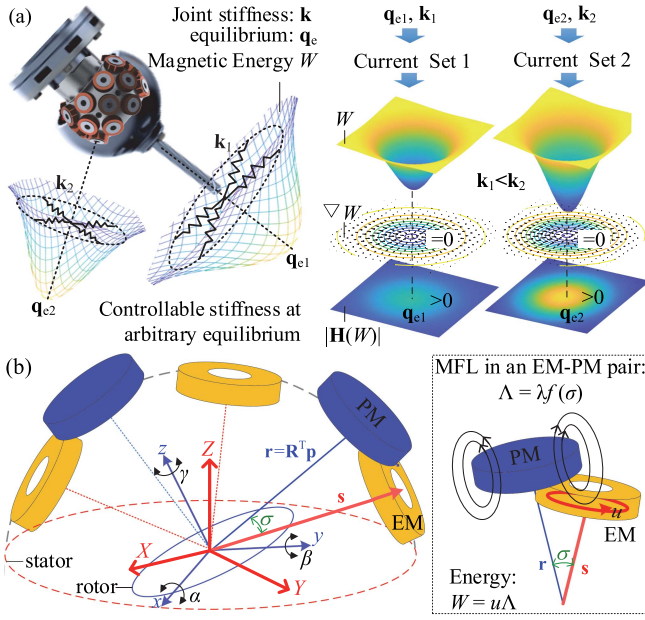
Fig. 2. Illustration of variable joint stiffness by magnetic energy shaping. (a) Variable joint stiffness at any desired equilibrium by magnetic energy shaping. (b) Illustration of pole configuration and magnetic flux linkage in EM-PM pairs.

stator and rotor frames, respectively. The EM poles are fixed in stator frame; and all the PM poles rotate with the rotor frame during motion where the rotor orientation is defined in terms of Euler angles (roll, pitch, yaw) $\mathbf{q} = [\alpha, \beta, \gamma]^T$. The rotation matrix can be expressed as (1) with respect to the stator frame

$$\mathbf{R}(\alpha, \beta, \gamma)$$
$$= \begin{bmatrix} C_\gamma C_\beta & -S_\gamma C_\beta & S_\beta \\ S_\gamma C_\alpha + C_\gamma S_\beta S_\alpha & C_\gamma C_\alpha - S_\gamma S_\beta S_\alpha & -C_\beta S_\alpha \\ S_\gamma S_\alpha - C_\gamma S_\beta C_\alpha & C_\gamma S_\alpha + S_\gamma S_\beta C_\alpha & C_\beta C_\alpha \end{bmatrix}. \quad (1)$$

In (1), S and C represent *sine* and *cosine* respectively. As illustrated in Fig. 2(b), for the SJM driven by the PM and EM poles, the magnetic flux linkage (MFL, based on which the magnetic energy is derived) in each EM-PM pair can be characterized as a function of the separation angle σ as (2) assuming the PMs and EMs are axis-symmetric

$$\Lambda = \lambda f(\sigma). \quad (2)$$

In (2), λ denotes the PM magnetization (with both magnitude and polarity); and the separation angle σ between the EM and the PM can be expressed as (3a) where $\mathbf{s}$ and $\mathbf{r}$ represent the unit vectors from the origin to the geometrical centers of the EM and PM respectively in *XYZ* frame

$$\sigma = \cos^{-1}(\mathbf{r} \cdot \mathbf{s}) \text{ where } \mathbf{r} = \mathbf{R}\mathbf{p}. \quad (3a\text{-}b)$$

In (3b), $\mathbf{p}$ is a constant vector representing coordinates of the PM vector $\mathbf{r}$ with respect to the local rotor frame *xyz*. The analytical solution for calculating the kernel function f (characterizing MFL of an EM-PM pair at different σ) in (2) can be found in [21].

As the magnetic energy stored in each EM equals to the product of the supplied current and the MFL [22], for an SJM consisting of N_E EMs and N_P PMs, the total magnetic energy stored in the SJM can be expressed as (4) as a sum of the magnetic energies stored in each EM, which can be computed based on the MFL obtained in (2)

$$W = \sum_{j=1}^{N_E} u_j \Lambda_j = \sum_{j=1}^{N_E} u_j \sum_{l=1}^{N_P} \lambda_l f(\sigma_{j,l}). \quad (4)$$

In (4), u_j denotes the current input in the jth EM (EM$_j$); and Λ_j is the total MFL in EM$_j$ contributed by all N_P PMs; λ_l is the magnetization of the lth PM (PM$_l$); $\sigma_{j,l}$ refers to the separation angle between EM$_j$ and PM$_l$.

For the scalar field W, as long as the gradients are zero at the desired equilibrium $\mathbf{q}_e$ and the Hessian matrix (consisting of secondary derivatives) is positive definite, W will be a convex field which has a local minimum at $\mathbf{q}_e$ [23] (as illustrated in Fig. 1(b)). Hence, according to the principle of minimum energy, the rotor will be driven to minimum energy point $\mathbf{q}_e$ automatically due to the formed W field as long as (5) is satisfied

$$\begin{cases} \nabla W|_{\mathbf{q}=\mathbf{q}_e} = \mathbf{0} \\ \mathbf{H}(W)|_{\mathbf{q}=\mathbf{q}_e} \succ 0 \end{cases}. \quad (5)$$

Meanwhile, based on the principle of virtual displacement [24], the gradient of the magnetic energy (with respect to the orientation) is equal to the magnetic torque $\boldsymbol{\tau}$; and the Hessian matrix by definition is equivalent to the stiffness matrix $\mathbf{k}$ of the motor, which can be expressed as

$$\nabla W = \frac{dW}{d\mathbf{q}} = \boldsymbol{\tau} \quad (6)$$

$$\mathbf{H}(W) = \frac{d}{d\mathbf{q}^T}\left(\frac{dW}{d\mathbf{q}}\right) = \frac{d\boldsymbol{\tau}}{d\mathbf{q}^T} = \mathbf{k}. \quad (7)$$

Equations (5)–(7) suggest that the motor torque and the torque gradients (equal to the motor stiffness $\mathbf{k}$) jointly determine the shape of the magnetic energy field. As long as a convex magnetic energy field is formed in the vicinity of an arbitrary rotor orientation, the equilibrium as well as the directional stiffness of the SJM is automatically set in an antagonistic sense. In order to provide a means to shape the magnetic energy in real-time, the relationship between the current inputs and the motor torque/stiffness is established in the subsequent section.

B. Relationship Among Currents, Motor Torque and Stiffness

According to (3a) and (3b), the separation angle $\sigma_{j,l}$ is $\mathbf{q}$-dependent. Substituting (4) into (6), (7), the magnetic torque $\boldsymbol{\tau}$ and the magnetic stiffness matrix $\mathbf{k}$ can be derived as

$$\boldsymbol{\tau} = \sum_{j=1}^{N_E} u_j \sum_{l=1}^{N_P} \lambda_l f'(\sigma_{j,l}) \frac{d\sigma_{j,l}}{d\mathbf{q}} \quad (8)$$

$$\mathbf{k} = \sum_{j=1}^{N_E} u_j \sum_{l=1}^{N_P} \lambda_l \left[f''(\sigma_{j,l}) \frac{d\sigma_{j,l}}{d\mathbf{q}} \frac{d\sigma_{j,l}}{d\mathbf{q}^T} + f'(\sigma_{j,l}) \frac{d^2\sigma_{j,l}}{d\mathbf{q}d\mathbf{q}^T} \right]. \quad (9)$$

In (8) and (9), $f' = df/d\sigma$, $f'' = d^2f/d\sigma^2$. Taking first and second derivatives of (3a) with respect to $\mathbf{q}$, the first and second derivatives of the separation angle $\sigma_{j,l}$ can be obtained as

$$\frac{d\sigma_{j,l}}{d\mathbf{q}} = -\frac{1}{\sin(\sigma_{lj})}\begin{bmatrix} \delta(\mathbf{R}_\alpha) \\ \delta(\mathbf{R}_\beta) \\ \delta(\mathbf{R}_\gamma) \end{bmatrix} \quad (10)$$

$$\frac{d^2\sigma_{j,l}}{d\mathbf{q}d\mathbf{q}^T} = -\frac{\cos(\sigma_{lj})}{\sin^3(\sigma_{lj})}$$

$$\begin{bmatrix} \delta(\mathbf{R}_\alpha)\delta(\mathbf{R}_\alpha) & \delta(\mathbf{R}_\alpha)\delta(\mathbf{R}_\beta) & \delta(\mathbf{R}_\alpha)\delta(\mathbf{R}_\gamma) \\ \delta(\mathbf{R}_\alpha)\delta(\mathbf{R}_\beta) & \delta(\mathbf{R}_\beta)\delta(\mathbf{R}_\beta) & \delta(\mathbf{R}_\beta)\delta(\mathbf{R}_\gamma) \\ \delta(\mathbf{R}_\alpha)\delta(\mathbf{R}_\gamma) & \delta(\mathbf{R}_\beta)\delta(\mathbf{R}_\gamma) & \delta(\mathbf{R}_\gamma)\delta(\mathbf{R}_\gamma) \end{bmatrix}$$

$$-\frac{1}{\sin(\sigma_{lj})}\begin{bmatrix} \delta(\mathbf{R}_{\alpha\alpha}) & \delta(\mathbf{R}_{\alpha\beta}) & \delta(\mathbf{R}_{\alpha\gamma}) \\ \delta(\mathbf{R}_{\alpha\beta}) & \delta(\mathbf{R}_{\beta\beta}) & \delta(\mathbf{R}_{\beta\gamma}) \\ \delta(\mathbf{R}_{\alpha\gamma}) & \delta(\mathbf{R}_{\beta\gamma}) & \delta(\mathbf{R}_{\gamma\gamma}) \end{bmatrix}. \quad (11)$$

In (10) and (11), $\mathbf{R}_{(.)} = \partial\mathbf{R}/\partial(.)$, $\mathbf{R}_{(.)(*)} = \partial^2\mathbf{R}/\partial(.)\partial(*)$; δ is an operator transforming a matrix into a scalar in the form of

$$\delta(\bullet) = \mathbf{s}_j^T(\bullet)\mathbf{p}_l. \quad (12)$$

In (12), the constant vectors $\mathbf{s}_j$ and $\mathbf{p}_l$ represent the pole coordinates of EM_j and PM_l, respectively,

Substituting (10), (11) into (8), (9), and rearranging the components of $\mathbf{k}$ into vector form, $\bar{\mathbf{k}}$ [1] the relationship between the energy field shape vector ε (consisting of motor torque and the stiffness vector) and the motor current input vector $\mathbf{u}$ can be obtained as

$$\varepsilon = \begin{bmatrix} \boldsymbol{\tau} \\ \mathbf{k} \end{bmatrix} = \begin{bmatrix} \mathbf{M} \\ \mathbf{N} \end{bmatrix}\mathbf{u} \quad (13)$$

where $\mathbf{M} = [\mathbf{m}_1(\mathbf{q}), \ldots, \mathbf{m}_j(\mathbf{q}), \ldots, \mathbf{m}_{N_E}(\mathbf{q})]$ (13a)

$$\mathbf{N} = [\mathbf{n}_1(\mathbf{q}), \ldots, \mathbf{n}_j(\mathbf{q}), \ldots, \mathbf{n}_{N_E}(\mathbf{q})] \quad (13b)$$

$$\mathbf{u} = [u_1, \ldots, u_j, \ldots, u_{N_E}]^T. \quad (13c)$$

For the jth EM, the components of $\mathbf{M}$ and $\mathbf{N}$ in (13a) and (13b) can be obtained in closed-form as (14a) and (14b), respectively, by substituting (10), (11) into (8), (9)

$$\mathbf{m}_j(\mathbf{q}) = -\sum_{l=1}^{N_P}\frac{\lambda_l f'(\sigma_{lj})}{\sin(\sigma_{lj})}\begin{bmatrix} \delta(\mathbf{R}_\alpha) \\ \delta(\mathbf{R}_\beta) \\ \delta(\mathbf{R}_\gamma) \end{bmatrix} \quad (14a)$$

$$\mathbf{n}_j(\mathbf{q}) = \sum_{l=1}^{N_P}\frac{\lambda_l}{\sin^3\sigma_{lj}}$$

$$\left\{\eta(\sigma_{lj})\begin{bmatrix} \delta(\mathbf{R}_\alpha)\delta(\mathbf{R}_\alpha) \\ \delta(\mathbf{R}_\beta)\delta(\mathbf{R}_\beta) \\ \delta(\mathbf{R}_\gamma)\delta(\mathbf{R}_\gamma) \\ \delta(\mathbf{R}_\alpha)\delta(\mathbf{R}_\beta) \\ \delta(\mathbf{R}_\beta)\delta(\mathbf{R}_\gamma) \\ \delta(\mathbf{R}_\gamma)\delta(\mathbf{R}_\alpha) \end{bmatrix} - \zeta(\sigma_{lj})\begin{bmatrix} \delta(\mathbf{R}_{\alpha\alpha}) \\ \delta(\mathbf{R}_{\beta\beta}) \\ \delta(\mathbf{R}_{\gamma\gamma}) \\ \delta(\mathbf{R}_{\alpha\beta}) \\ \delta(\mathbf{R}_{\beta\gamma}) \\ \delta(\mathbf{R}_{\alpha\gamma}) \end{bmatrix}\right\} \quad (14b)$$

[1] $\mathbf{k} = \frac{d\boldsymbol{\tau}}{d\mathbf{q}^T} \in \Re^{3\times3}$ is reduced to $\bar{\mathbf{k}} = \left[\frac{\partial^2 W}{\partial\alpha^2}, \frac{\partial^2 W}{\partial\beta^2}, \frac{\partial^2 W}{\partial\gamma^2}, \frac{\partial^2 W}{\partial\alpha\partial\beta}, \frac{\partial^2 W}{\partial\beta\partial\gamma}, \frac{\partial^2 W}{\partial\alpha\partial\gamma}\right]^T \in \Re^{6\times1}$ as $\frac{\partial^2 W}{\partial\alpha\partial\beta} = \frac{\partial^2 W}{\partial\beta\partial\alpha}, \frac{\partial^2 W}{\partial\alpha\partial\gamma} = \frac{\partial^2 W}{\partial\gamma\partial\alpha}, \frac{\partial^2 W}{\partial\beta\partial\gamma} = \frac{\partial^2 W}{\partial\gamma\partial\beta}$ for a continuous field.
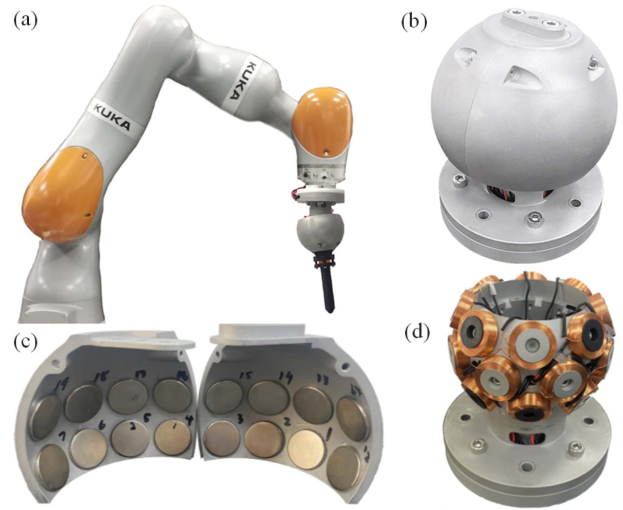

Fig. 3. Prototype SJM. (a) Robot with a SJM wrist. (b) SJM overview. (c) Rotor embedded with PMs. (d) Stator housing EMs.

where $\eta(\sigma_{lj}) = f''(\sigma_{lj})\sin\sigma_{lj} - f'(\sigma_{lj})\cos\sigma_{lj}$ (14c)

and $\zeta(\sigma_{lj}) = f'(\sigma_{lj})\sin^2\sigma_{lj}$ (14d)

Hence, (13) provides closed-form relationship between the energy shape vector ε and current input $\mathbf{u}$. Given a desired shape vector $\varepsilon_d = [\tau_d, \mathbf{k}_d]^T$ consisting of the desired torque and stiffness at the desired equilibrium $\mathbf{q}_e$, an optimal current input vector $\mathbf{u}$ can be computed in the form of pseudoinverse using (15) for the SJM with redundant inputs ($N_E > 9$)

$$\mathbf{u} = \begin{bmatrix} \mathbf{M} \\ \mathbf{N} \end{bmatrix}^T\left(\begin{bmatrix} \mathbf{M} \\ \mathbf{N} \end{bmatrix}\begin{bmatrix} \mathbf{M} \\ \mathbf{N} \end{bmatrix}^T\right)^{-1}\varepsilon_d. \quad (15)$$

When the motor is supplied with the current inputs computed using (15), a convex magnetic energy field can be formed and the rotor will be constrained by the magnetic field at the specified equilibrium $\mathbf{q}_e$ with an intrinsic joint stiffness of $\mathbf{k}_d$.

III. SJM PROTOTYPE DESIGN AND TESTS

An SJM prototype has been developed and equipped on a robotic manipulator (*Kuka iiwa*) for test. As shown in Fig. 3, the SJM is mounted on the distal end of the manipulator operating as a dexterous wrist with omnidirectional motion and intrinsic compliance. The torque mode of the manipulator is disabled in all the tests. The motor size and weight as well as the PM/EM pole configurations are summarized in Table I. The motor parameters including the PM magnetizations and EM current densities were calibrated and validated following the procedures presented in [22]. The dynamic model of the proposed SJM can be derived as

$$\mathbf{M}(\mathbf{q})\ddot{\mathbf{q}} + \mathbf{C}(\mathbf{q}, \dot{\mathbf{q}})\dot{\mathbf{q}} + \mathbf{g}(\mathbf{q}) = \boldsymbol{\tau} + \boldsymbol{\tau}_e. \quad (16)$$

In (16), $\mathbf{M}(\mathbf{q})$ is the rotor inertia matrix; $\mathbf{C}(\mathbf{q}, \dot{\mathbf{q}})\dot{\mathbf{q}}$ is the combined centripetal and Coriolis torque vector; $\mathbf{g}(\mathbf{q})$ is the gravitational torque vector; $\boldsymbol{\tau}$ and $\boldsymbol{\tau}_e$ are the electromagnetic

TABLE I
SJM PARAMETERS

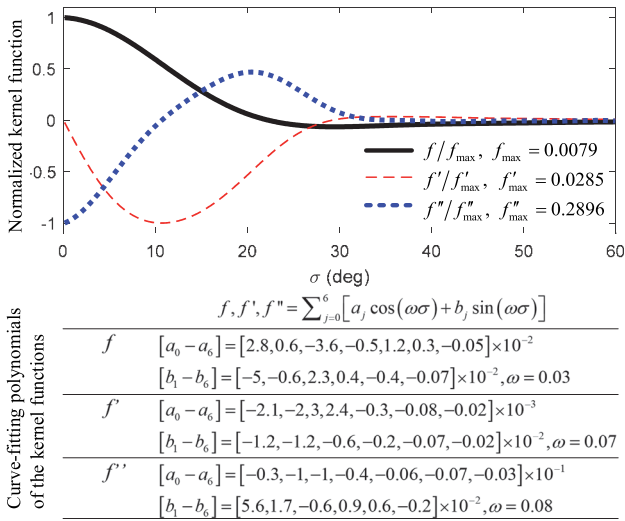| Motor specifications:			
SJM size: 100mm in diameter, weight: 1.2kg			
Maximum torque: 1.5Nm (continuous), 4Nm(peak)			
Range of motion: α (-30°,30°), β (-30°,30°), γ (−∞, +∞)			
Rotor mass properties: m = 0.484 kg, h_z=6.937 mm			
$I_a = 606.43 \times 10^{-6}$ kg·m^2, $I_t = 847.34 \times 10^{-6}$ kg·m^2			
Rotor-PM dimensions and locations (in spherical coordinate R, Θ, Φ)			
	$a_o = 20$ *mm, l = 5 mm*, magnetization: $\mu_0 M_0 = 1.465$ *T*		
	Index(*l*)	(Θ,Φ) *in xyz*	*Polarity*
PM_l centroid	1~12	105° (*l*-1) × 30° + 15°	$(-1)^l$
$R_P = 45.5$ *mm*	13~24	75° (*l*-13) × 30°+ 15°	$(-1)^{l-1}$
Stator-EM dimensions and locations (in spherical coordinate R, Θ, Φ)			
	$a_o = 20$ *mm*, $a_i = 8$ *mm, l = 6 mm*, *wire dia.*: *d* = 0.3 *mm*		
	Index(*j*)	(Θ,Φ) *in xyz*	
	1~8	115°	(*j*-1) × 45°
EM_j centroid	9~16	65°	(*j*-9) × 45° + 22.5°
$R_E = 38.31$ *mm*	17~24	90°	(*j*-17) × 45°

Fig. 4. Numerical results and curve-fitting parameters of kernel function *f* (magnetic flux linkage) and its first/second derivatives.

driving torque and the external torque applied on the rotor, respectively. The detailed formulation can be found in [22].

When the gravitational torque (which contributes to the potential energy similar to the magnetic energy) is taken into consideration, (5) can be rewritten as (17) to form a convex potential energy at equilibrium $\mathbf{q}_e$, and the desired shape vector ε_d can be specified by taking into account of the rotor gravity

$$\begin{cases} \nabla W = \boldsymbol{\tau} + \mathbf{g} = 0 \\ \mathbf{H}(W) = \dfrac{d\boldsymbol{\tau}}{d\mathbf{q}^{\mathrm{T}}} + \dfrac{d\mathbf{g}}{d\mathbf{q}^{\mathrm{T}}} \succ 0 \end{cases}. \tag{17}$$

As an illustration, the kernel function *f* and its first and second derivatives for computing the **M**, **N** components in (14a) and (14b) have been numerically computed as a function of the PM-EM separation angle as shown in Fig. 4. Note that the numerical results are normalized with respect to the peak values. To assist real-time implementation of (14a) and (14b), curve-fitting functions with closed-form expressions are obtained based on the numerical values where the polynomial coefficients are also summarized in Fig. 4. For illustration, the implementation
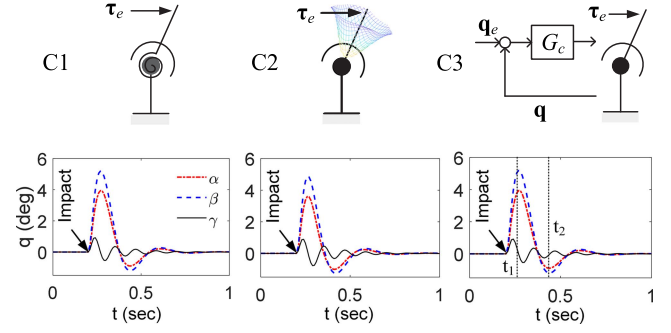

Fig. 5. Comparison of three compliant joint configurations and their rotor responses to impulsive external torques.

procedures for realizing a desired joint stiffness $\mathbf{k}_d$ at a desired equilibrium $\mathbf{q}_e$ are summarized as follows.

1) Calculate the components in (14a) and (14b) using the curve-fitting functions shown in Fig. 4 with separation angles calculated with (3a) at the desired equilibrium orientation $\mathbf{q}_e$.
2) Specify a desired shape vector $\boldsymbol{\epsilon}_d = [\boldsymbol{\tau}_d, \boldsymbol{k}_d]^T$ consisting of a desired torque $\boldsymbol{\tau}_d$ (to compensate for the gravitational torque in (16) and a desired joint stiffness matrix $\mathbf{k}_d$.
3) Compute the desired current input vector **u** with (15).
4) Supply the currents into the EMs with current amplifiers.

A. Simulation: Joint Compliance Comparisons

The effectiveness of the proposed SJM with magnetic energy shaping method is validated. Specifically, three configurations for achieving joint compliance (see Fig. 5) are compared as follows.

1) C1-Ideal Joint Spring: Ideal spring that can provide stiffness in all directions with the form

$$\boldsymbol{\tau}_{\text{spring}} = \mathbf{k}_{c1}\tilde{\mathbf{q}} \tag{18}$$

where $\mathbf{k}_{c1}$ is the stiffness matrix and $\tilde{\mathbf{q}}(= \mathbf{q} - \mathbf{q}_e)$ is the joint deflection from the equilibrium. Note that an ideal joint spring with linear stiffness in omnidirection is not applicable in practice and it is only used in this simulation to provide the reference responses of an ideal intrinsic compliant joint.

2) C2-Energy Shaping: Joint compliance is achieved through the proposed SJM with a joint stiffness matrix equal to $\mathbf{k}_{c2}$. The currents for delivering the desired torque shape vector are computed using (15).

3) C3-Impedance Control: Impedance control law (19a) with feedback of the joint angle is used to provide joint compliance (C3 in Fig. 4), which leads to the desired impedance in (19b) by substituting (19a) into the dynamic model in (16)

$$\boldsymbol{\tau} = \mathbf{M}\ddot{\mathbf{q}} + \mathbf{C}(\mathbf{q}, \dot{\mathbf{q}})\dot{\mathbf{q}} + \mathbf{g}(\mathbf{q}) - \mathbf{k}_{c3}\tilde{\mathbf{q}} \tag{19a}$$

$$\boldsymbol{\tau}_e = \mathbf{k}_{c3}\tilde{\mathbf{q}}. \tag{19b}$$

The computation process of current input for generating the desired torque determined by (19a) can be found in [2].

In this simulation, an impulsive external torque is applied on the rotor shaft as shown in Fig. 5 at 0.2 s with a magnitude of
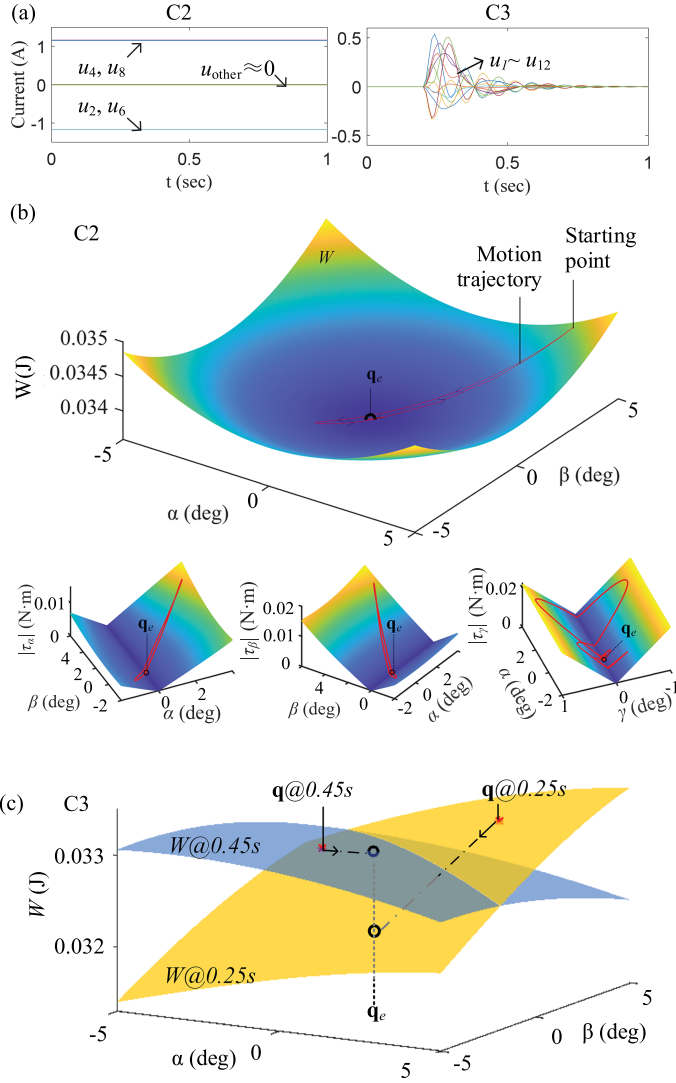
Fig. 6. Illustration of currents and potential energy fields for C2 and C3. (a) Current inputs. (b) Illustration of total energy field W and torque components in C2. (c) Illustration of energy field W and motion states (at 0.25 and 0.45s) in C3.

0.2 Nm. The desired joint stiffness matrices ($\mathbf{k}_{c1}$, $\mathbf{k}_{c2}$, $\mathbf{k}_{c3}$) in all three cases are set as an diagonal matrix diag(0.3,0.3, 2.5) and the equilibrium is set at $\mathbf{q}_e = [0,0,0]^T$. Fig. 5 compares the simulated responses for all three configurations. The rotor motions in all three cases show very similar dynamic responses when subject to an impulse torque, which demonstrates that the joint driven with both the energy shaping method and the impedance control can provide equivalent joint compliance that an ideal joint spring delivers. As C1 is not applicable in practice, the subsequent simulations focus on comparing C2 and C3 in terms of computational efficiency and robustness.

Fig. 6 compares the computed current input and the resultant energy field for C2 and C3. The computational periods for C2 and C3 are 2.25 and 2.36 ms, respectively, (based on *MATLAB 2023b*). Note that even if C2 and C3 cost comparable computational time in one cycle, C2 with intrinsic compliance only need to execute once for a desired equilibrium while C3 based
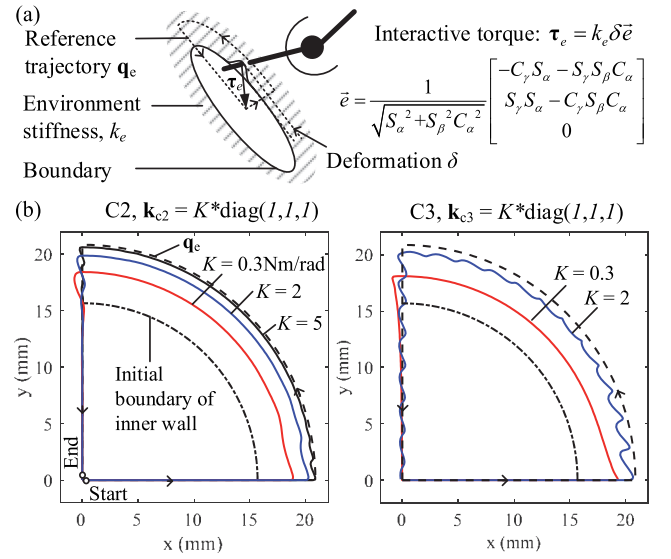

Fig. 7. Illustration of joint robustness during contact with unstructured environment. (a) Simulation configuration, environment stiffness $k_e = 0.35$ N·m/rad. (b) Comparison of joint responses. The inner wall is pressed from its initial boundary (dotted line) towards the reference $\mathbf{q}_e$ (dashed line) and the solid lines denote the actual trajectories with different joint stiffness.

on feedback requires instantaneously update of control torque and currents in each cycle [see Fig. 6(a)].

To demonstrate the effectiveness of the energy shaping method, the formed energy field is plotted in Fig. 6(b) in (α, β) space where the simulated rotor motion trajectory is superimposed; the components of the torque applied on the rotor are also shown in Fig. 6(b). The results show that a minimum energy point is formed at the desired equilibrium $\mathbf{q}_e$ with a constant set of current inputs computed using the proposed energy shaping method. The rotor starting from any point will automatically converge to $\mathbf{q}_e$ (see the motion trajectory in Fig. 6(b) without feedback control. Antagonistic torque is applied on the rotor at the equilibrium in all directions (see the torque components in Fig. 6(b).

As a comparison, the potential energy fields of the joint with the impedance control in C3 are plotted in Fig. 6(c). Note that as the impedance control supplying time-varying currents based on simultaneous feedback, the energy field are also time-varying. To assist visualization, the energy profiles were plotted at two time stamps for C3 in Fig. 6(c) ($t_1 = 0.25$ s and $t_2 = 0.45$ s as denoted in Fig. 4). It can be seen that the potential field formed in C3 cannot guarantee the stability of $\mathbf{q}_e$ at each sampling cycle ($\mathbf{q}_e$ is not the lowest point in the vicinity). Although asymptotic convergence can be guaranteed to certain extent by continuously changing the energy field based on real-time feedback, the contact instability may occur especially when the feedback system is subject to sensor bandwith/noises or the system in contact with unknown environment.

The difference in robustness of C2 and C3 is best illustrated with Fig. 7 where the responses of the rotor shaft for interacting with unstructured environment are simulated. As shown in Fig. 7(a), the rotor shaft is commanded to follow a reference trajectory $\mathbf{q}_e$ (1/4 circle counter-clockwise as denoted by the

dashed line) to make contact with the inner wall of a target (with stiffness k_e). When the shaft presses the target, a reaction force normal to the boundary is applied on the shaft which translates into an interactive torque [see Fig 7(a)].

Fig. 7(b) presents the simulated responses for the joint driven by C2 and C3, respectively, when different stiffness are specified. Specially, the reference trajectory is followed by C2 by continuously changing the equilibrium. It can be seen that compliant interactions can be guaranteed for both C2 and C3 when the joint stiffness is small. However, when the joint stiffness increases (larger than that of the environment stiffness), unstable contact can be observed for C3 at $K = 2$. C2 with intrinsic joint compliance provides better robustness in contact with unstructured environment and the joint stiffness can be flexibly specified in a much larger range.

B. Experiments

The capability of the SJM with energy shaping method for providing a compliant omnidirectional robotic joint are experimentally investigated. The proposed energy shaping algorithms have been deployed onto a DSP-based controller (*TI, C2000*) with an execution period of 5 ms. The currents were supplied with a 12-channel driver (with embedded current loop). The orientation of the wrist was recorded by an inertial measurement unit sensor (IMU, *Glonavin MY530HE*).

1) Variable Stiffness/Equilibrium Test: The variable joint stiffness with the proposed method have been experimentally tested where the configurations as well as the results are presented in Fig. 8.

As shown in the figure, the rotor shaft is positioned at different orientations around a specified equilibrium and the magnetic restoring torque were measured with a torque sensor (*ATI Mini40*) at steady-state. The tests were conducted at two different equilibria ($\mathbf{q}_{e1}$, $\mathbf{q}_{e2}$) with three different stiffness values. Fig. 8(b)–(c) presents the components of the restoring torque as functions of joint angles at $\mathbf{q}_{e1}$ and $\mathbf{q}_{e2}$, respectively. The results show that the joint stiffness can be precisely controlled and the torque linearity is within 5% in 10° range (±5°) in the vicinity of each equilibrium in all directions. To illustrate the relationship between the joint stiffness and the shape of W, Fig. 8(d) and (e) plots the W profiles and current inputs supplied into the EMs at $\mathbf{q}_{e1}$ for different specified joint stiffness. It can be seen that steeper W field with larger torque gradient $\mathbf{k}_d$ leads to larger joint stiffness (with larger currents). The energy fields in Fig. 8(d) and (e) also imply that the equilibrium is unique in α–β domain for the formed convex field. As the EM/PM poles have a repetitive distribution in the spinning direction (with a 60° period), the stiffness will present periodic patterns in γ-direction. Therefore, when the joint is pushed out of the 60° range in γ-direction by external forces, it will stabilize at next equilibrium in the neighborhood. In practice, the stiffness can be increased at the boundary to constrain the joint or the equilibrium can be continuously changed to move the effective stiffness range.
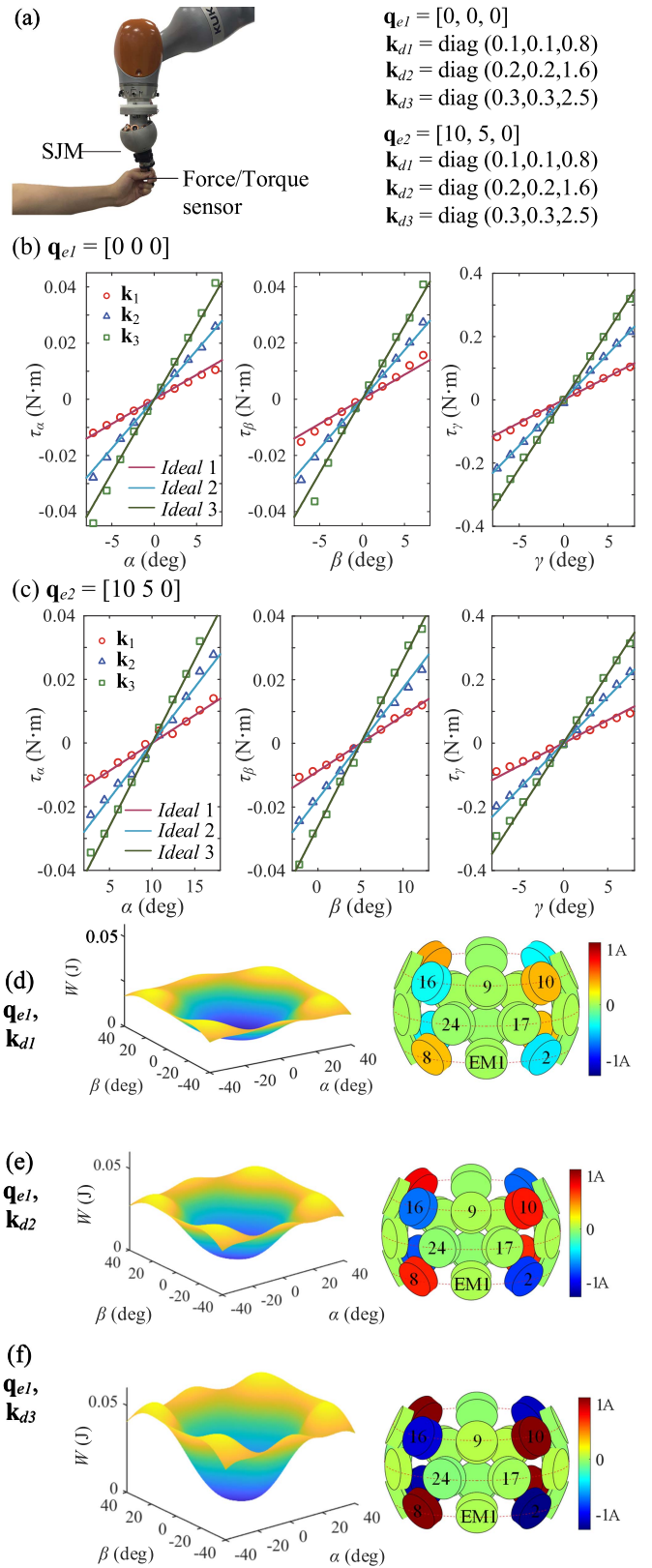

Fig. 8. Controllable joint stiffness at arbitrary equilibrium. (a) Experimental configuration. (b) Restoring torque at $\mathbf{q}_{e1} = [0\ 0\ 0]$. (c) Restoring torque at $\mathbf{q}_{e2} = [10\ 5\ 0]$. (d)–(f) illustration of energy W and current inputs for $\mathbf{k}_{d1}$, $\mathbf{k}_{d2}$, $\mathbf{k}_{d3}$ at $\mathbf{q}_{e1}$, respectively.
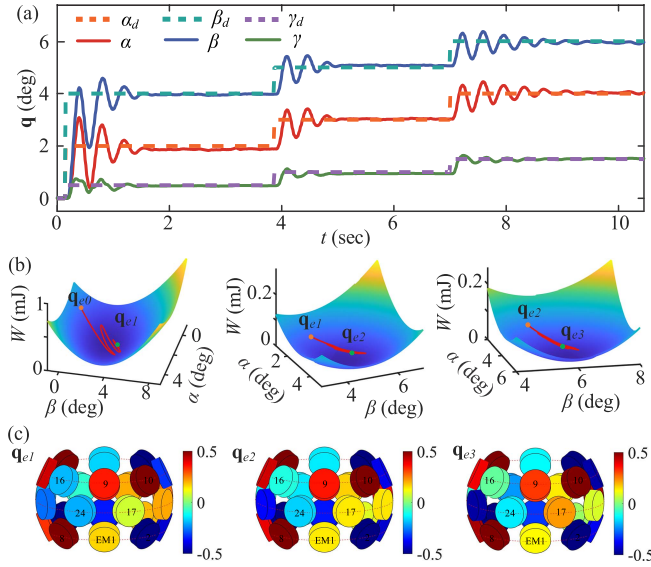
Fig. 9. Point-to-point variation of equilibrium, $\mathbf{k}_d = \text{diag}(0.1,0.1,0.8)$. (a) Euler angle responses. (b) Energy fields and motion trajectories. (c) Current inputs at $\mathbf{q}_{e1}$, $\mathbf{q}_{e2}$, $\mathbf{q}_{e3}$.

TABLE II
OPEN-LOOP SPECIFICATIONS

Step		Rise time (s)	Settling time (s)	S-S error (degs)
$\mathbf{q}_{e0}$ $[0,0,0]^T$ to $\mathbf{q}_{e1}$ $[2,4,0.5]^T$	α	0.09	1.11	0.1304
	β	0.12	1.11	0.0334
	γ	0.045	0.705	0.0217
$\mathbf{q}_{e1}$ $[2,4,0.5]^T$ to $\mathbf{q}_{e2}$ $[3,5,1]^T$	α	0.06	0.81	0.0314
	β	0.075	0.66	0.0767
	γ	0.075	0.12	0.0546
$\mathbf{q}_{e2}$ $[3,5,1]^T$ to $\mathbf{q}_{e3}$ $[4,6,1.5]^T$	α	0.075	1.335	0.0359
	β	0.09	1.2	0.0461
	γ	0.06	0.12	0.0104

2) Point-to-Point Variation of Equilibrium: The rotor orientation can be regulated at different positions by changing the equilibrium of the SJM. Fig. 9(a) presents the rotor responses when the equilibrium was sequentially changed from an initial orientation $\mathbf{q}_{e0}$ to three different orientations $\mathbf{q}_{e1}$, $\mathbf{q}_{e2}$, $\mathbf{q}_{e3}$ (see Table II). Fig. 9(b) and (c) plots the magnetic energy field W and the current inputs in the EMs at $\mathbf{q}_{e1}$, $\mathbf{q}_{e2}$, $\mathbf{q}_{e3}$ where the motion trajectories are superimposed.

The experimental results suggest that the equilibrium can be changed to arbitrary orientation to accomplish point-to-point motion for robotic joints. The open-loop specifications given in Table II show that the rotor can be quickly changed from one equilibrium to another with rise time less than 0.1 seconds and settling time less than 1.4 s.

The robustness of point-to-point response was also tested. Fig. 10(a) presents the joint response for a 46° step change in the desired equilibrium. Fig. 10(b) presents the joint response when a step change was commanded while the rotor was still in the oscillations from previous step change. The results demonstrate that the joint with energy shaping method is capable of providing robust point-to-point response when the system is subject to large and abrupt inputs.
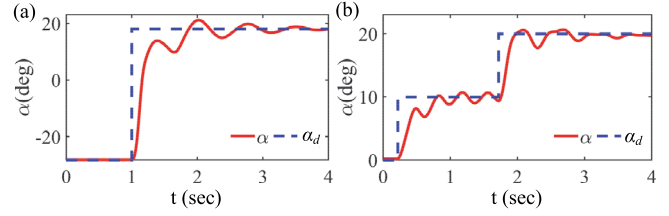

Fig. 10. Illustration of point-to-point robustness, $\mathbf{k}_d = \text{diag}(0.1,0.1,0.8)$. (a) 46° step. (b) Step change in transient phase.
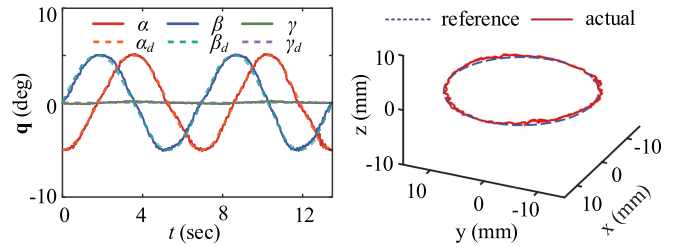

Fig. 11. Trajectory tracking responses of the SJM, reference orientation $\mathbf{q}_d = [5\sin t, 5\cos t, 0]$, execution time/cycle = 5 ms, joint orientation on left and end-effector trajectory on right.

3) Continuously Changing Equilibrium for Trajectory Tracking: As the current inputs for controlling the magnetic energy are obtained in closed-form in (15), the magnetic energy of the SJM can be shaped in real-time which allows for dynamically change of the joint stiffness and equilibrium. Fig. 11 presents the responses for the end-effector to track a desired circular trajectory by continuously changing the rotor equilibrium. The orientation of the wrist was measured by the IMU and the position of the end-effector was recorded using (3b). During the test, a torque in the following form has been complemented in a feedforward sense to compensate the dynamics of the rotor

$$\boldsymbol{\tau}_0 = \mathbf{M}(\mathbf{q}_d)\ddot{\mathbf{q}}_d + \mathbf{C}(\mathbf{q}_d, \dot{\mathbf{q}}_d) + \mathbf{G}(\mathbf{q}_d).$$

The execution time per cycle during the test was 5 ms. The real-time responses of the joint orientation and the trajectory of the end-effector shown in Fig. 10 demonstrates that the desired trajectory can be tracked in real-time with good precision using the proposed method, which also permits the SJM to perform motion-based tasks.

IV. DEMONSTRATIONS

The feasibility of a robotic manipulator equipped with a SJM for accomplishing compliant manipulations is validated in the following two demonstrations.

A. Peg-in-Tilt-Hole With SJM Wrist (No Force Sensor)

The capability of dealing with compliant operation of the robotic manipulator equipped with a SJM wrist is tested in a peg-in-hole operation (see Fig. 12). Unlike conventional robots relying on force/torque sensors for performing peg-in-hole operations, the SJM enables a robot to accomplish the task with a
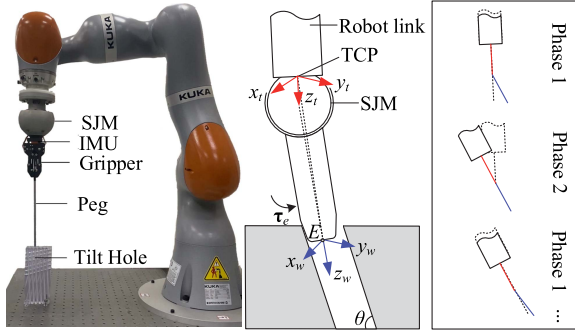
Fig. 12. Peg-in-tilt-hole with SJM-based robotic wrist. $x_ty_tz_t$ denotes the coordinate of the TCP. $x_wy_wz_w$ represents the wrist coordinate.

Fig. 13. Robot wrist responses in peg-in-hole test, hole #1 has a tilt angle around 5-deg, hole #2 has a tilt angle around 10°. (a) Wrist inclination angle as a function of the TCP moving distance (b) Recorded TCP displacement during the insertion. (c) Captured robot poses at initial and final states (for hole #1).

compliant wrist where the equilibrium/stiffness can be flexibly configured.

Fig. 12 presents the experimental setup and schematically illustrates the peg-in-hole process. As shown in the figure, a gripper for picking up the pegs is installed on the robot wrist. The goal is to insert the pegs into the tilt holes (with tilt angles varying from 5° to 10°) in the workpiece. $x_ty_tz_t$ denotes the co-ordinate attached to the tool center point (TCP, the position and orientation can be directly controlled by the robot controller); $x_wy_wz_w$ represents the wrist coordinate in which the gripper/peg is fixed. As illustrated in Fig. 12, the peg-in-hole operation with a robot equipped with a SJM wrist is proposed in a two-phase procedure:

1) *Phase 1. Reach and Bend:* The robot TCP is controlled to reach along z_t-axis so that the tip of the peg (with lead angle) gets into the tilt hole. The peg is bent during the reaching phase which lead the wrist to passively rotate due to the interaction torque τ_e between the peg and the workpiece.

2) *Phase 2. Adjust Robot Pose:* The orientation of the TCP is controlled to rotate around the end point E to align z_t with z_w, where the orientation of the wrist is recorded by the IMU.

The two-phase process is executed repeatedly until the peg is fully inserted into the tilt hole. Fig. 13 presents experimental results for insertions into two holes with different tilt angles. Fig. 13(a) and (b) present the responses of the wrist angle and the displacement of the TCP, respectively. To assist visualization, the captured images of the robot poses at the initial state and the final state are shown in Fig. 13(c). The results demonstrate that the robotic wrist enables the peg to comply with the holes and successfully lead the robot to adjust the pose to finish the insertion process into holes with different angles (around 5° and 10°, respectively, in this demonstration). The SJM with the proposed insertion regime eliminates the need of force/torque sensors and can be applied for holes with a large range of tilting angles without any teaching or prior-knowledge-based programming.

B. Shape/Stiffness Perception in Unstructured Environment

It is essential for robots to detect the stiffness of interactive targets to ensure stable contact in unstructured environment
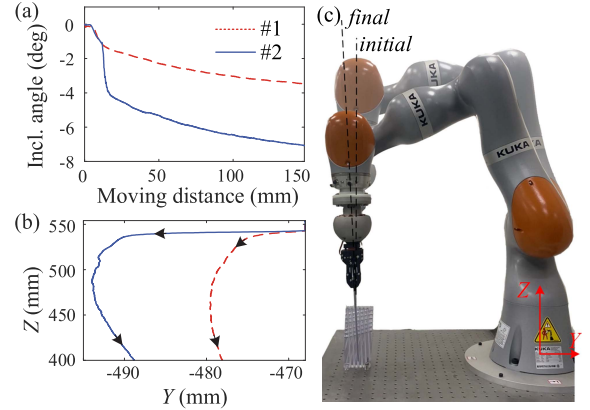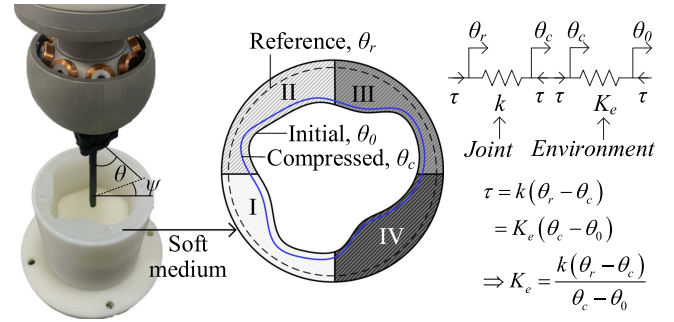

Fig. 14. Interaction with unstructured target. The inner wall is composed of four sectors filled with medium in different stiffness: I (ecoflex, HS-00-10), II(ecoflex, HS-00-30), III(ecoflex, HS-00-50), IV(dragon-skin, HS-A-10). More grey level represents higher hardness.

[25], [26]. The feasibility of the robot with SJM for perceiving the shape and the stiffness of an unstructured target is also demonstrated. Fig. 14 presents the experimental setup where a finger driven by the SJM wrist is used to detect the target. The interior body of the target is segmented into four sections each filled with soft materials with different hardness (the materials and the nominal hardness are denoted in Fig. 14). To assist understanding, the task is best defined in task space with altitude and azimuth angles (θ, ψ). The relationship between the task space variables and the Euler angles in wrist space can be expressed as (20a-b) as illustrated in Fig. 14

$$\theta = \arccos\left(C_\beta C_\alpha\right), \quad \psi = \arccos\left(S_\beta/S_\theta\right). \quad (20a\text{-}b)$$

The detection process is characterized by two procedures.

1) Shape Perception With Low Joint Stiffness: The robotic wrist is first set with low stiffness ($k = 0.3$) to detect the interior shape of the target. The task is performed for the wrist to follow a reference trajectory (θ_r, as illustrated in Fig. 14) by specifying continuous equilibria in the task space. It is assumed that the detected interior shape is approximately close to its original shape of the target when the wrist stiffness is very low.

2) Stiffness Perception With High Joint Stiffness: The wrist is set to high joint stiffness ($k = 0.8$) to detect the stiffness of the
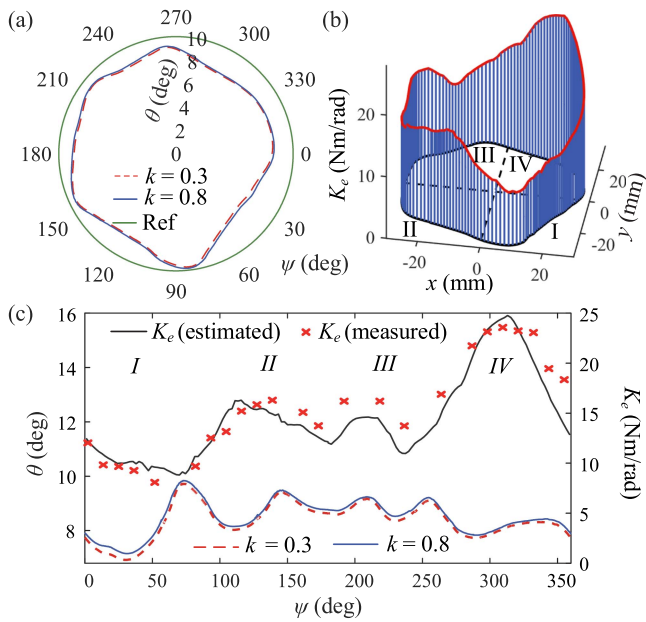
Fig. 15. Shape and stiffness detection results. (a) Detected boundaries in task space (θ, ψ) when the target interact with the wrist at different joint stiffnesses. (b) Estimated stiffnesses of the target (c) deformed boundaries and estimated/measured stiffness.

target by following the same reference trajectory. The interior wall is compressed by the finger when the wrist performs the scanning motion in the task space. The compressed trajectory is recorded which is used to estimate the stiffness of the target. The relationship among the joint stiffness (k), target stiffness (K_e), the initial boundary (θ_0), the compressed boundary (θ_c), and the reference trajectory (θ_r) are derived in Fig. 14.

Fig. 15(a) presents the detected inner boundaries of the target when interacting with the SJM under different joint stiffness. Note that the interior body is compressed towards the radial direction when the joint stiffness is set at a higher value. The estimated stiffness of each section of the target are shown in Fig. 15(b). To assist visualization, the detected boundaries and the stiffness are also plotted as a function of the azimuthal angle ψ in Fig. 15(c). Fig. 15(c) also compares the estimated stiffness and the stiffness measured with a force gauge, which show good agreement (with mean percentage error less than 20%). The results show that the proposed method offers an effective means for dynamically detecting and perceiving the unstructured environment and stable contact can be ensured due to the intrinsic compliance of the SJM when interacting with object in different stiffness.

V. CONCLUSION

This article proposed a SJM for robots capable of multi-DOF motion in one joint and variable stiffness in omnidirections. An energy shaping method by simultaneously controlling both motor torque and torque gradients with motor currents was proposed, which allows for independently changing the equilibrium and the joint stiffness without any elastic elements or force/torque based feedback control. A prototype SJM was

developed and tested. The results show that desired joint stiffness was well rendered around any specified equilibrium which was also continuously changed for tracking motion. A 5% stiffness linearity can be guaranteed in a 10° range in all directions. The SJM equipped on a Kuka robotic manipulator as a compliant wrist has shown good performances in peg-in-hole tests without force/torque sensors (with hole tilting angle larger than 10°). The SJM wrist also demonstrated the capability of perceiving shape and stiffness of unstructured environment with perception error less than 20%.

Based on the capability of manipulating the stiffness and equilibrium of an omni-directional joint, it was beneficial to smartly plan the motion-stiffness configurations in order to improve the efficiency as well as the interactive performances of the proposed motor. Therefore, our future work will explore planning algorithms for the proposed motor to provide enhanced robotic joint with smart and robust interactive manipulations.

REFERENCES

[1] M. J. Kim, A. Werner, F. Loeffl, and C. Ott, "Passive Impedance control of robots with viscoelastic joints via inner-loop torque control," *IEEE Trans. Robot.*, vol. 38, no. 1, pp. 584–598, Feb. 2022.

[2] K. Bai, W. Chen, K.-M. Lee, Z. Que, and R. Huang, "Spherical wrist with hybrid motion-impedance control for enhanced robotic manipulations," *IEEE Trans. Robot.*, vol. 38, no. 2, pp. 1174–1185, Apr. 2022.

[3] J. Reinecke, A. Dietrich, A. Shu, B. Deutschmann, and M. Hutter, "A robotic torso joint with adjustable linear spring mechanism for natural dynamic motions in a differential-elastic arrangement," *IEEE Robot. Automat. Lett.*, vol. 7, no. 1, pp. 9–16, Jan. 2022.

[4] G. Grioli et al., "Variable stiffness actuators: The user's point of view," *Int. J. Robot. Res.*, vol. 34, no. 6, pp. 727–743, May 2015.

[5] S. Wolf et al., "Variable stiffness actuators: Review on design and components," *IEEE/ASME Trans. Mechatron.*, vol. 21, no. 5, pp. 2418–2430, Oct. 2016.

[6] F. Petit, A. Dietrich, and A. Albu-Schäffer, "Generalizing torque control concepts: Using well-established torque control methods on variable stiffness robots," *IEEE Robot. Automat. Mag.*, vol. 22, no. 4, pp. 37–51, Dec. 2015.

[7] N. Hogan, "Impedance control: An approach to manipulation: Part I—Theory, part II—Implementation, part III—Applications," *J. Dyn. Syst., Meas. Control*, vol. 107, pp. 1–24, Mar. 1985.

[8] F. Ficuciello, L. Villani, and B. Siciliano, "Variable impedance control of redundant manipulators for intuitive human-robot physical interaction," *IEEE Trans. Robot.*, vol. 31, no. 4, pp. 850–863, Aug. 2015.

[9] A. Dietrich and C. Ott, "Hierarchical impedance-based tracking control of kinematically redundant robots," *IEEE Trans. Robot.*, vol. 36, no. 1, pp. 204–221, Feb. 2020.

[10] R. V. Ham, T. G. Sugar, B. Vanderborght, K. W. Hollander, and D. Lefeber, "Compliant actuator designs," *IEEE Robot. Automat. Mag.*, vol. 16, no. 3, pp. 81–94, Sep. 2009.

[11] M. Grebenstein et al., "The hand of the DLR hand arm system: Designed for interaction," *Int. J. Robot. Res.*, vol. 31, no. 13, pp. 1531–1555, 2012.

[12] B. Vanderborght et al., "Exploiting natural dynamics to reduce energy consumption by controlling the compliance of soft actuators," *Int. J. Robot. Res.*, vol. 25, no. 4, pp. 343–358, 2006.

[13] D. J. Braun et al., "Robots driven by compliant actuators: Optimal control under actuation constraints," *IEEE Trans. Robot.*, vol. 2, no. 5, pp. 1085–1101, Oct. 2013.

[14] Y.-L. Yu and C.-C. Lan, "Design of a miniature series elastic actuator for bilateral teleoperations requiring accurate torque sensing and control," *IEEE Robot. Automat. Lett.*, vol. 4, no. 2, pp. 500–507, Apr. 2019.

[15] H. Chang, S. J. Kim, and J. Kim, "Feedforward motion control with a variable stiffness actuator inspired by muscle cross-bridge kinematics," *IEEE Trans. Robot.*, vol. 35, no. 3, pp. 747–760, Jun. 2019.

[16] N. Paine, S. Oh, and L. Sentis, "Design and Control Considerations for High-Performance Series Elastic Actuators," *IEEE/ASME Trans. Mechatron.*, vol. 19, no. 3, pp. 1080–1091, Jun. 2014.

[17] K. Bai et al., "Regulation and tracking control of omni-directional rotation for spherical motors," *IEEE Trans. Ind. Electron.*, vol. 70, no. 2, pp. 1696–1705, Feb. 2023.

[18] M. Shi, Q. Wang, G. Li, J. Xu, Q. Han, and Q. Ye, "A new adaptive analytical model for the spherical reluctance motor based on hybrid trigonometric function-power function," *IEEE Trans. Ind. Electron.*, vol. 70, no. 6, pp. 6099–6109, Jun. 2023.

[19] K. Bai, H. Yan, and K.-M. Lee, "Robust control of a spherical motor in moving frame," *Mechatronics*, vol. 75, 2021, Art. no. 102548.

[20] H. Li, Y. Zhao, B. Li, G. Li, and L. Cui, "Torque calculation of permanent magnet spherical motor based on virtual work method," *IEEE Trans. Ind. Electron.*, vol. 67, no. 9, pp. 7736–7745, Sep. 2020.

[21] K. Bai, K.-M. Lee, and J. Lu, "A magnetic flux model based method for detecting multi-DOF motion of a permanent magnet spherical motor," *Mechatronics*, vol. 39, pp. 217–225, 2016.

[22] K. Bai and K.-M. Lee, *Permanent Magnet Spherical Motors: Model and Field Based Approaches for Design, Sensing and Control*. Berlin, Germany: Springer, 2018.

[23] S. Boyd and L. Vandenberghe, *Convex Optimization*. Cambridge, U.K.: Cambridge Univ. Press, 2004.

[24] D. Cheng, *Field and Wave Electromagnetics*. London, U.K.: Pearson, 2007.

[25] Z. Liu, H. Jin, Y. Liu, and J. Zhao, "An online stiffness estimation approach for variable stiffness actuators using lever mechanism," *IEEE Robot. Automat. Lett.*, vol. 7, no. 3, pp. 6709–6717, Jul. 2022.

[26] A. Fagiolini, M. Trumi, and K. Jovanovi, "An input observer-based stiffness estimation approach for flexible robot joints," *IEEE Robot. Automat. Lett.*, vol. 5, no. 2, pp. 1843–1850, Apr. 2020.

Qianhong Xiao received the B.S. and M.S. degrees in mechanical engineering from the School of Mechanical Science and Engineering, Huazhong University of Science and Technology, Wuhan, China, in 2018 and 2021, respectively, where he is currently working toward the Ph.D. degree in mechanical engineering.

His research interests include dexterous electromagnetic actuators and medical robots.

Zehui Wang received the B.S. degree in mechanical engineering from Huazhong University of Science and Technology (HUST), Wuhan, China, in 2022.

He is currently a Graduate Student with the State Key Laboratory of iMET, HUST. His research interests include medical robots and smart actuators.

Chenjie Liu received the B.S. degree in mechanical design manufacturing and automation from Sichuan University, Chengdu, China, in 2023. He is currently working toward the Ph.D. degree in mechanical engineering with Huazhong University of Science and Technology, Wuhan, China.

His research interests include mechatronic design, control systems and robotics.

Mengke Li received the B.S. degrees in mechanical engineering from Chongqing University, Chongqing, China, in 2020 and the M.S. degree in mechanical engineering from Huazhong University of Science and Technology (HUST), Wuhan, China, in 2023.

He was a Graduate Research Assistant with the State Key Laboratory of Intelligent Manufacturing Equipment and Technology, HUST and his research interests include smart actuator design and control. He is currently a Robotics Systems Engineer with Shanghai United Imaging Healthcare Company Ltd, Shanghai, China.

Kun Bai (Member, IEEE) received the B.S. degree in control science and engineering from Zhejiang University, Hangzhou, China, in 2006, and the M.S. and Ph.D. degrees in mechanical engineering from the Woodruff School of Mechanical Engineering, Georgia Institute of Technology, Atlanta, GA, USA, in 2009 and 2012, respectively.

He is currently a Professor with the State Key Laboratory of iMET, Huazhong University of Science and Technology, Wuhan, China. His research interests include smart electromagnetic actuators/sensors and novel applications in robotics. Dr. Bai is Technical Editor for IEEE/ASME TRANSACTION ON MECHATRONICS. He was the recipient of ASME DSCD Mechatronics TC Best Paper Award in 2019.